Research Square

Preprints are preliminary reports that have not undergone peer review.
They should not be considered conclusive, used to inform clinical practice,
or referenced by the media as validated information.

A hidden hierarchy of compressive failure in carbon fibres

Stephen Eichhorn

s.j.eichhorn@bristol.ac.uk

University of Bristol

Cameron Woodgate

Imperial College

David Anthony

Imperial College London

Christopher Jones

University of Bristol

Milo Shaffer

Imperial College London

Article

Keywords:

Posted Date: November 10th, 2026

DOI: https://doi.org/10.21203/rs.3.rs-11483311/v1

License: This work is licensed under a Creative Commons Attribution 4.0 International License.
Read Full License

Additional Declarations: No competing interests reported.

A hidden hierarchy of compressive failure in carbon fibres

Cameron G. Woodgate[a,b], David. B. Anthony[b,c], Christopher P. Jones[d],
Stephen J. Eichhorn[a]*, Milo S. P. Shaffer[b,c]*

[a] *Bristol Composites Institute, School of Civil, Aerospace and Design Engineering, University of Bristol, University Walk, Bristol, BS8 1TR, UK.*

[b] *Department of Chemistry, Imperial College London, White City Campus, London, W12 0BZ, UK.*

[c] *Department of Materials, Imperial College London, South Kensington Campus, London, SW7 2AZ, UK.*

[d] *Interface Analysis Centre, School of Physics, H. H. Wills Physics Laboratory, University of Bristol, Bristol, BS8 1TL, UK.*

Fibre reinforced polymer composites dominate demanding structural applications due to their exceptional mechanical characteristics at low weights. However, their compressive strength is much lower than their tensile strength, limiting performance and wider deployment. While composite compression failure typically involves meso-scale fibre microbuckling and kink-band formation, the underlying compressive failure mechanisms of the reinforcing carbon fibres themselves are poorly understood, yet increasingly important in high modulus applications. Here, the three-dimensional internal structure of compressive failure within individual high-modulus carbon fibres is resolved using a new correlative nanoscale resolution serial-sectioning methodology. Reconstruction of failed fibres reveals previously unobserved internal nano-kink bands within single filaments, exposing a hidden hierarchy in which a characteristic composite-scale compressive instability re-emerges within the fibre microstructure itself. These nano-kink bands challenge the conventional view of fibre compression failure as a simple bulk shear fracture event and instead indicate a localised instability coupled to the fibre skin-core microstructure. They highlight a self-similar compression failure mechanism occurring both the meso- and nanoscale, separated by two orders of magnitude. Three-dimensional imaging additionally reveals Mode I fibre-matrix debonding, crack bifurcation, and wedge formation that map onto distinct stages of the fibre failure trajectory. These previously hidden interactions establish direct structural links between fibre microstructure and compressive failure, providing new insight into the origins of compression sensitivity in high-modulus carbon fibres and identifying potential pathways towards improved compressive performance in next-generation composite materials.

Carbon fibre reinforced polymer composites (CFRPs) are high performance materials, offering high specific strength and stiffness, driving applications in automotive, aerospace, marine, and sporting

* Corresponding Authors: Email: s.j.eichhorn@bristol.ac.uk, m.shaffer@imperial.ac.uk

goods industries. CFRPs owe their excellent mechanical properties in tension to their fine, fibrillar, generally continuous carbon reinforcing phase. The micron-scale diameters of individual carbon fibres (CFs) (typically 5-10 μm) limit defect sizes, create toughening mechanisms, and enable processing across multiple length scales to maximise (anisotropic) properties. Polymer matrices support the reinforcing fibres, transfer load between them and protect them from damage. Although many configurations are possible, composite components are most typically built from stacked layers of directionally aligned fibres, known as laminae, which together form a laminate.

Whilst CFRPs often have exceptional tensile properties, they suffer from poor compressive performance; the compressive strength of unidirectional fibre reinforced composites can be less than 60% of the same material's tensile strength[1]. This penalty may significantly limit composite designs, and undermines their high specific strength benefit, in compressive critical applications. For example, improving CFRP compressive performance is especially important for wind-turbine blade spar caps, where compressive strength limits material utilisation; previous optimisation studies indicate that a 25% or greater increase in compression strength could reduce spar-cap material cost by more than 50%, compared with an industry baseline[2].

Compression failure of carbon fibre (CF) composites involves multiple mechanisms at varying length scales, from matrix yielding, though fibre-matrix interfacial failure[3] and fibre fragmentation, to delamination and ultimately translaminar fracture. Fibre 'kink bands' are a widely recognised feature of compressive composite failure, caused by critical shear instability of the composite[1] (sometimes termed 'micro-buckling'), leading to local fibre rotation and fracture. The reduced compression performance of composites is usually attributed to this meso-scale, matrix-dominated mechanism, which is nominally independent of fibre strength[4]. However, in fact, composite failure modes also depends on the fibre type, often distinguished as 'high strength' (HS) or 'high modulus' (HM) fibres. HS fibres (<400 GPa) typically undergo matrix shear yielding and subsequent microbuckling failure[5] whereas HM fibres (>400 GPa) undergo a fibre-dominated fragmentation failure mode[6]. HM fibre composites are limited by their inherently low compressive strength along the fibre axis, restricting their use in compression-critical structural components[7]. This transition between matrix and fibre dominated failure modes is not always appreciated, and the links between internal fibre microstructure and intrinsic fibre compression performance are poorly understood. Here, a new focused ion beam scanning electron microscopy (FIB-SEM) serial block face imaging protocol is developed to explore single carbon fibre compression failure at an unprecedented nanometre resolution.

Microstructure and compressive failure of single carbon fibres

Despite measurement challenges, it is clear that intrinsic single CF strengths are also lower in compression than tension. Interestingly, reduced composite compression performance may not,

therefore, be attributable only to mesoscale ‘micro-buckling’. The knockdown in intrinsic compression strength is generally greater in HM than HS fibres (**Fig. 1**a). For example, for the fibres studied in detail below, the ratio of compressive to tensile strengths decreases from 0.74 for AS4, a HS fibre (tensile modulus 231 GPa), to 0.42 for M55J, a HM fibre (540 GPa). This divergence indicates an underlying change of mechanism, as well as a dependence of compressive failure behaviour on fibre microstructure.

Polyacrylonitrile (PAN) precursor-based carbon fibres dominate the market (>90%)[8]; they exhibit complex, heterogeneous microstructures comprising planar assemblies of graphene sheets oriented approximately parallel to the fibre axis[9]. Structural hierarchy is present at the micro- to nanoscales (**Fig. 1**b), consisting of anisotropic turbostratic carbon, with graphitic sp^2-bonded crystallite domains interspersed within amorphous, disordered sp^3 bonded carbons, alongside anisotropic pores and voids[10–12]. Carbon fibres can thus be considered composite materials, in their own right, comprising reinforcing graphitic crystallites and a disordered carbon matrix that supports the crystallites, distributing the load. The PAN fibre spinning process often also generates radial heterogeneities[13], commonly known as “skin-core” structures. The outer “skin” typically contains larger, well-aligned graphitic crystallites, less disordered carbon, and larger needle-like voids[9,14,15], whereas the inner “core” contains smaller, more misoriented crystallites, more disordered carbon, and smaller, more numerous voids[16].

Preferred crystallographic orientation strongly influences mechanical and thermal properties. Some alignment of the graphitic planes parallel to the fibre axis generally enhances both tensile stiffness and strength[11]. However, the trend in tensile strength reverses at higher orientations, due to the presence of larger defects and the effects of transverse splitting, leading to relatively lower strength for HM fibres (**Fig. 1**a)[17]. Similar trends are observed in compressive strength, but only weakly due to measurement challenges[3], and are poorly understood.

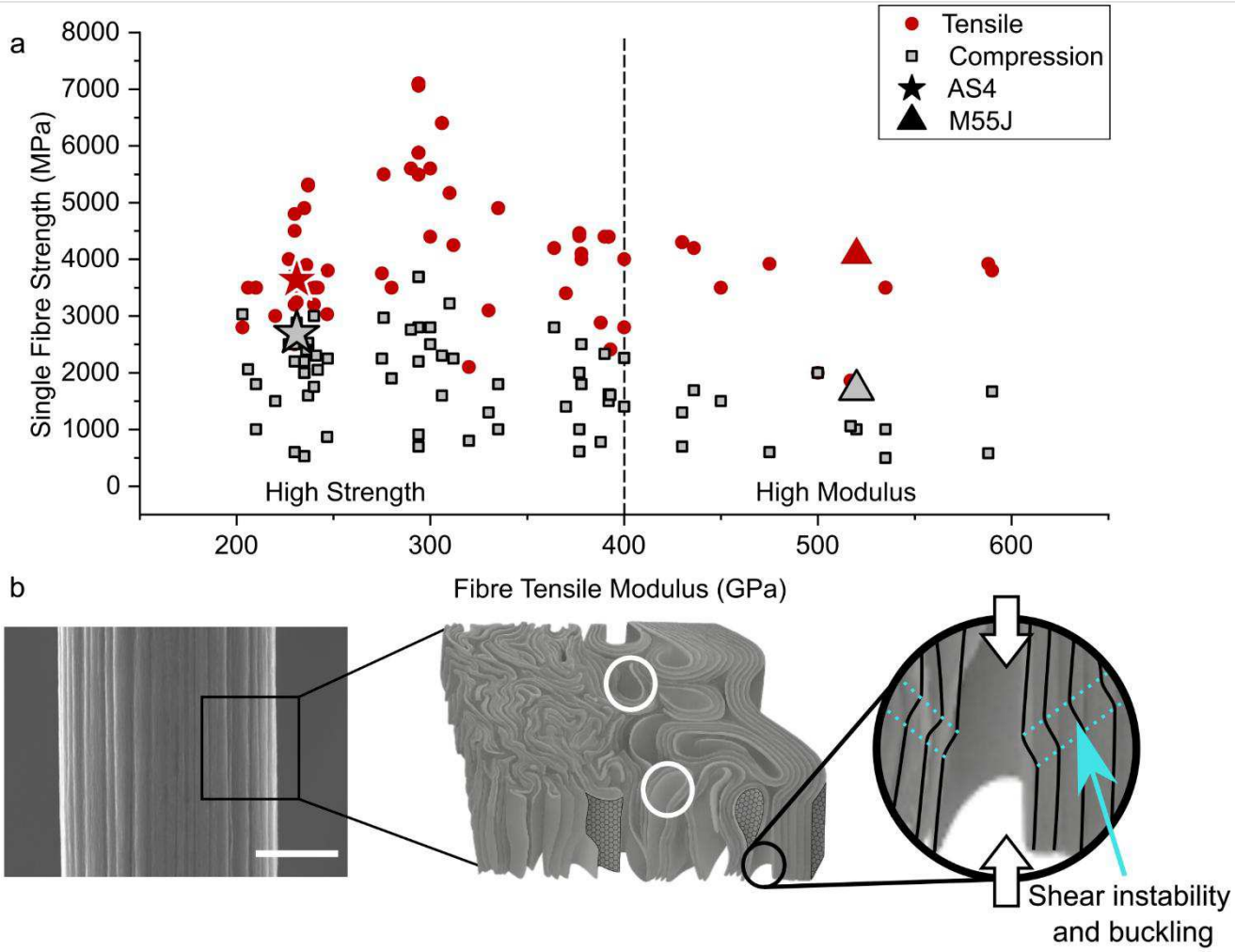


Fig. 1 | Compressive behaviour changes with fibre microstructure. a. Literature values for tensile and compressive strengths for a range of single PAN-based carbon fibres, highlighting a deviation in the ratio (strength:modulus) at higher strengths, with a dotted line indicating an approximate modulus transition point from 'high strength' fibres to 'high modulus; the fibres investigated here (AS4 & M55J) are highlighted. References for these data can be found in Supplementary Information Table S1. b. Scanning electron microscopy image of a single high modulus (HM; M55J) carbon fibre, with a schematic representation of a 3D high modulus fibre microstructure, adapted from[18], with potential defects and voids highlighted with circles, and a schematic of shear instability driven microstructural nanobuckling of graphitic planes within a fibre. Scale bar is 2 μm.

In compression, CFs typically display a non-linear stress–strain response at higher strains, sometimes described as "modulus softening", which is a reversible phenomenon usually attributed to reversible rotation of graphitic crystallites[19,20], within the more amorphous, 'disordered' matrix. Tension may increase graphitic alignment, leading to stiffening, but the effect tends to be very weak and is generally not a significant design consideration. In CFRPs, fibre failure is often categorised and oversimplified as a bulk "crushing[1]" or "shear failure", where the whole fibre yields at a critical

maximum shear stress, resulting in a break at 45° to the fibre axis. However, in more detailed single fibre studies, failure has been hypothesised to relate to a microstructure-controlled instability process, attributed variously to microbuckling or kinking of microfibrils/crystallites, separation or sliding of turbostratic graphite layers, and local buckling of graphitic carbon layer stacks[21]. In the latter framework, compressive strength has been proposed to depend on the buckling stress of carbon layer stacks in transversely unsupported regions adjacent to microvoids, with the unsupported span governed by the longitudinal microvoid [21,22] (**Fig. 1**b right). Although lacking direct evidence, this model provides a useful nanoscale analogue to composite-scale Argon-Budiansky microbuckling and kink-band analyses: in composites, misaligned fibres become unstable within a shearing matrix, whereas within carbon fibres, graphitic carbon layer stacks act as the reinforcing elements which become unstable[4].

These shear instability effects remain to be evidenced and must be modulated by the complex (heterogeneous) internal fibre microstructure. We propose that fibre failure is driven by a localised shear instability in the fibre skin, where crystallite shear strength and modulus is at a minimum due to large crystallite sizes, higher alignment and large defects, which then propagates into the fibre core. The ongoing response after initial fibre failure is particularly relevant to composite compressive performance, since load can continue to transfer across broken ends, subject to evolving damage. We previously quantified localised stress states in HM PAN-based fibres during compressive fragmentation, using Raman-based stress mapping[6], and hypothesised a possible mode I tensile opening interfacial debonding mechanism. Progressive compressive fragmentation has also been shown to contribute to pseudo-ductile behaviour in hybrid composites, providing new routes to notch insensitivity[23]. Here, we explore the 3D structures that evolve during single CF compression failure, considering the trajectory from initial fragmentation to the ongoing evolution at increasing strain.

Micron-scale fibre failure mechanisms

Since fibre-based failure modes manifest most clearly in HM composites, we first consider an archetypical HM PAN fibre (M55J, tensile modulus 540 GPa), using a single fibre model composite geometry (Fig. S1, Supplementary Information). In our previous study, optical microscopy (OM) and *in situ* Raman stress mapping (*is*RSM) identified compressive fragmentation with characteristic failure features (**Fig. 2**a), first appearing as surface “microcracks” (**Fig. 2**a i) at 0.5 % compressive strain, and 2.1 ± 0.1 GPa fibre stress[19]. With increasing deformation, the initial surface features evolve into a range of characteristic damage structures, including a “shear-like” break (**Fig. 2**a ii) with associated (mode I) interface debonding (**Fig. 2**a iii); wedge-type features may also appear, following secondary fractures (**Fig. 2**a iv), and further contribute to the opening displacement during fragment movement. These features correlate with distinctive stress distributions along the fibre axis[6] (shown schematically in **Fig. 2**b). Since the crack appears at approximately 45° to the fibre’s

longitudinal axis (see **Fig. 2**a ii), it is tempting to assume a shear failure, *i.e.* the failure occurring at the location of the maximum shear stress. However, since *is*RSM only probes the fibre surface, and at moderate (~1 um) spatial resolution, the mechanisms of internal fibre failure, at the sub-micron level, were unknown. We, therefore, developed a new approach to three-dimensional reconstruction of the failed microstructure.

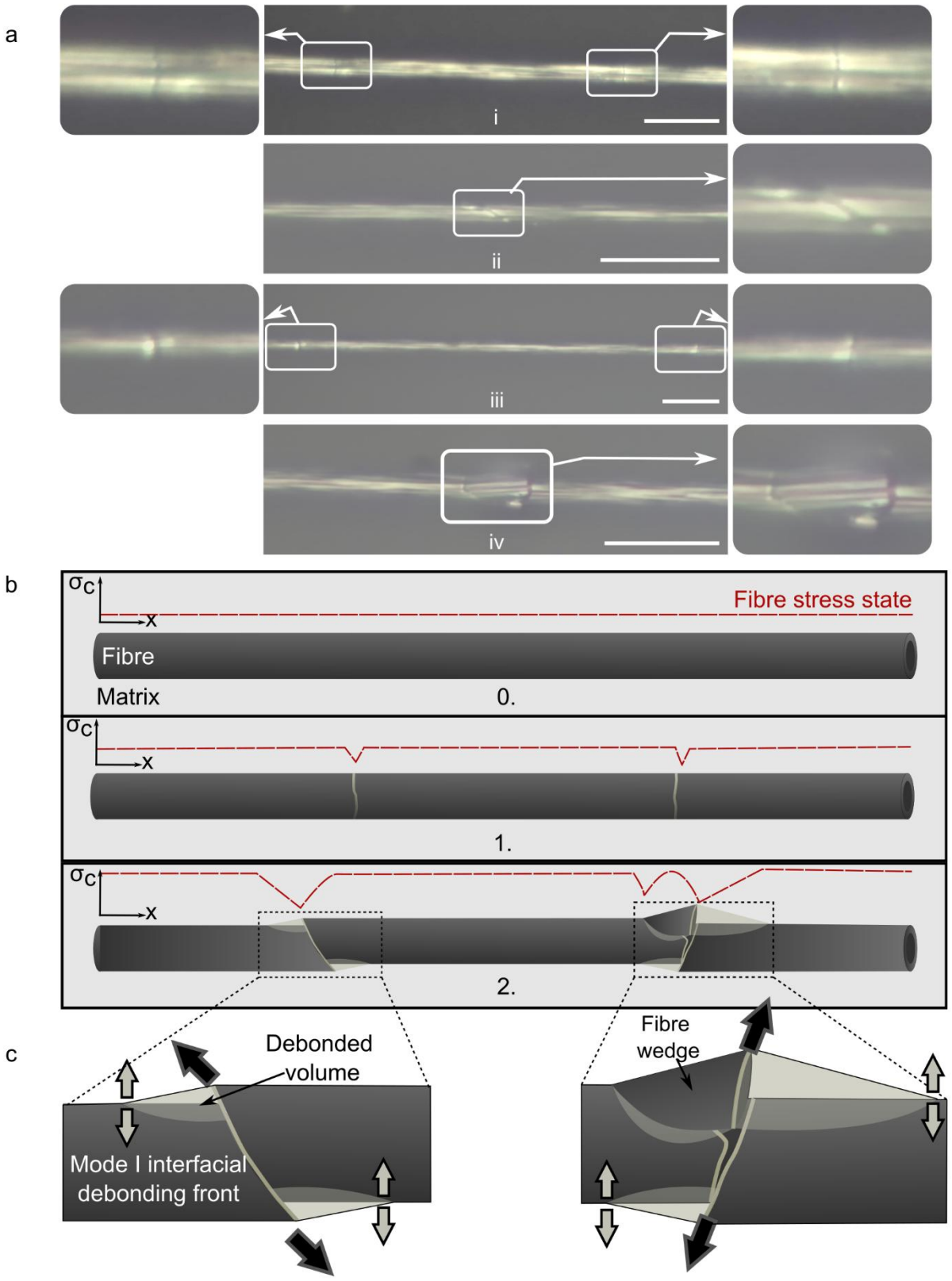


Fig. 2 | Features of high modulus carbon fibre breaks observed in compression with Raman spectroscopy and optical microscopy. a. Optical microscopy images of features of compressive failure, i. Microcrack features of compressive break initiation, typically observed early on during compressive fragmentation. ii, “shear-like” break feature commonly observed in carbon fibre compression fracture, oriented at 45° to the longitudinal fibre axis. iii, Fibre break lines with neighbouring apparent debonded regions, appearing as brighter areas due to presumed internal

scattering of light. iv, Inter-fragment 'wedge' feature observed and predicted to form during fragmentation, ejected during fragment evolution. b. Schematic of single HM fibre compressive fragmentation depicting observed and predicted fragmentation behaviour with corresponding local stress state, with microcrack initiation in 1. and shear-like and wedge formation behaviour depicted in 2. Mode I interfacial debonding mechanism illustrated. c. Highlighted predicted mechanisms occurring during HM fibre fragmentation. Scale bars in a are 5 mm and for optical microscope images in b are 20 μm. Schematic dimensions are not to scale.

FIB-SEM driven serial block face (SBF) imaging is a powerful technique for determining 3D microstructures with sub-20nm resolution; here, it has been applied, for the first time, to study fractured carbon fibres in unprecedented detail. Suitable representative breaks within single fibre model composites were identified by OM and transferred to high resolution SBF imaging. Due to a thin (<30 μm) layer of encapsulating epoxy, the fibres are not visible using standard SEM imaging, requiring a marking methodology for correlative imaging (see methods section). The resulting three-dimensional SBF reconstruction (**Fig. 3**a) provides a top-down projection (*xz* projection, Supplementary Information Fig. S2b and S3b) to complement the raw detector in-plane images (*xy* projection, Fig. S2b, 3b), revealing the post-failure geometry of individual compressive breaks in a HM fibre. In this example, the fibre contains a crack inclined at ~47° to the fibre axis, in which failure initiated at 2.2 GPa at 0.5% matrix strain[6,19], with the sample being further deformed to 1.25 % matrix strain.

The 3D reconstruction confirms the schematic phenomena inferred from the 2D, low resolution optical microscopy and *is*RSM (**Fig. 2**b), but revealing additional detail for both "simple" (**Fig. 3** left) and "compound" (**Fig. 3** right) fractures. The proposed movement of the fibre, following the simple "shear-like" failure (**Fig. 3**a), has created a large void in the matrix around the fibre (570 μm^3 in **Fig. 3**), evidence of the Mode I push-off ('peeling') interfacial debonding predicted, but not observed, previously[6]. The shape of the void reflects the unloading relaxation prior to imaging. The debonding is asymmetric around the rotational axis of the fibre (**Fig. 3**) due to asymmetric motion of the fragments, as shown schematically in **Fig. 3**c. Although the fracture extends across the whole fibre, the end faces remain in frictional contact, consistent with axial compression stress transfer observed via *is*RSM[6]. In-plane friction presumably contributes to the constraint of post-failure motion, alongside matrix plasticity constraints, and the resistance to interfacial crack opening. Mode I interfacial debonding is not observed during tensile deformation, where interfacial yielding is thought to take place via mode II shear[24].

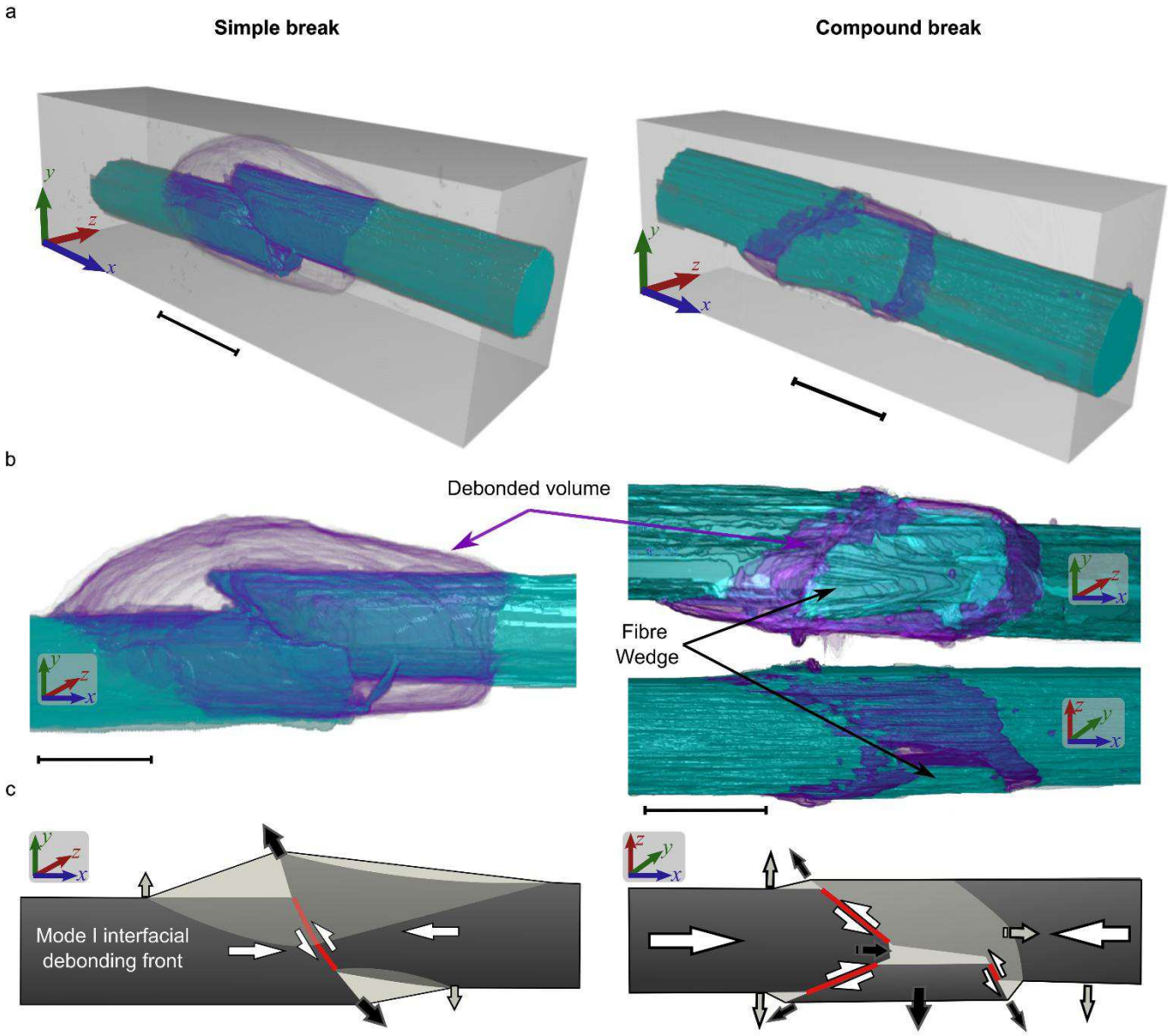


Fig. 3 | Reconstructions of HM fibre breaks with both simple (left) and compound (right) breaks. a, Reconstructed 3D volume with fibre (blue), matrix (grey) and void (purple) phases segmented, features of interest highlighted in b. c, Schematic illustrating the post-compressive behaviour of the fibre, including fragment movement and interfacial debonding mechanisms, with red indicating frictional contact. All scale bars, 5 μm. High-modulus PAN-based fibres (M55J) fragment in compression at 0.5 ± 0.03% strain (corresponding to 2.1 ± 0.1 GPa fibre stress[19]), with this sample deformed to 1.25 % strain.

Some fragmentation events display a compound, bifurcated morphology, with an associated 'wedge' feature, in which a section of the fibre is ejected (**Fig. 3** right). The wedge feature shown, approximately 7.0 × 3.4 × 1.3 μm, is consistent with estimates, by OM, ~ 10 μm in 2D projection[6]. We previously inferred the formation of wedge features from low resolution OM[6], however, their appearance is rarely mentioned in the literature[25]. Fibre wedges are observed via isRSM to form in the mid stages of failure evolution, as the section of fibre separates from the bulk fibre, the wedge

becomes an independent ‘fibre’ fragment gaining a stress profile independent to that of the bulk fibre (**Fig. 2**b step 2). SBF imaging now confirms the existence of wedge features that become separated from the bulk fibre, and reveals richer internal details, including longitudinal internal fibre splitting and the relative depth of the wedge (*z* axis) across the fibre’s diameter (1.3 μm in the case of **Fig. 3**).

The formation of the wedge feature is associated with a reduced debonded length and smaller debonded volume, as part of the strain energy normally driving Mode I debonding is instead consumed by the bifurcation of the fracture plane. Although the debonded geometry still indicates Mode I behaviour is occurring, its extent is diminished relative to the simple fracture. A key advantage of the 3D SBF image reconstruction is that it enables debonding to be quantified volumetrically, rather than only through linear debonded lengths, providing access to debonded volumes that have not previously been measured in compressive failure. The two fracture modes, simple and compound (**Fig. 3**), show different debonded volumes (70 *cf. 5*70 μm³), despite forming at different locations in the same specimen, taken to the same final compressive matrix strain (1.25 %). However, the two breaks did not necessarily initiate at the same strain. As in tension, local compression strength is expected to vary stochastically along the fibre length due to the distribution of microstructural defects[27]. *is*RSM shows that much of the remaining fragment length continues to sustain increasing axial stress after initial fibre fracture[6], due both to interfacial stress transfer (as in tension) and to direct fibre end contact. The intersection of the strength variation with the stress distribution drives progressive fragmentation events at increasing applied strains (from 0.5 – approximately 1.0 %), and hence strain energies. Complex, bifurcated crack paths are typically associated with a critical energy release rate or when a dynamic fracture condition is exceeded[26]. Earlier fibre breaks are, therefore, more likely to be simple fractures, leading to progressive fibre displacement over a larger strain range, increasing interfacial opening and debond volume. Later breaks are more likely to form complex fracture morphologies to alleviate larger accumulated strain energies (a more extreme example is discussed below for AS4 fibres). Nevertheless, simple fractures may still evolve into complex ones due to secondary events, as observed in *is*RSM, particularly if displacement of the simple fracture surface is constrained.

Nano-scale internal fibre failure mechanisms

To understand the role of fibre microstructure in HM fibre fracture, single filaments were deformed to a lesser extent past damage initiation (0.5 %) and imaged at high resolution, in three dimensions, using the new FIB SEM methodology (**Fig. 4**a-b). At intermediate strains, the internal fibre structure remained intact, unlike the samples deformed to complete fragment disconnection at higher strains (**Fig. 3**). The “skin-core” structure of the fibre is resolved and clearly plays an important role in the damage progression, since the outer skin is broken, whilst the core remains partly connected. While

the core exhibits pronounced localised rotation, fragments near the surface are separated without evidence of rotation (**Fig. 5**), indicating the presence of a skin–core structure with distinct failure mechanisms. The diameter of the kink band and associated core region, approximately 3.4 to 4.7 μm, is consistent with reported core diameters in PAN-based fibres[28], typically 2.7 to 5.5 μm.

The internal failure geometry bears a striking and surprising resemblance to multi-fibre kink bands observed during compressive failure of macroscopic composites[29], as illustrated in **Fig. 4**c, though at around two orders of magnitude smaller length scale. Surface indications of kink bands have been observed, at modest resolution, in other fibres, particularly in pitch-based carbon[30] and aramids[31], but not in PAN-based fibres or resolved in 3D. The internal fibre “nano-kink band” is a distinct, localised region of internal structural rotation, appearing as a diagonal band spanning much of the fibre diameter (**Fig. 5**). It consists of locally rotated fibre ligaments separated by nanoscale voids, with average ligament lengths and widths of approximately 430 nm and 190 nm, respectively. The kink band ligaments are separated by nanoscale inter-ligament voids that form near-continuous horizontal channels across much of the kink band thickness.

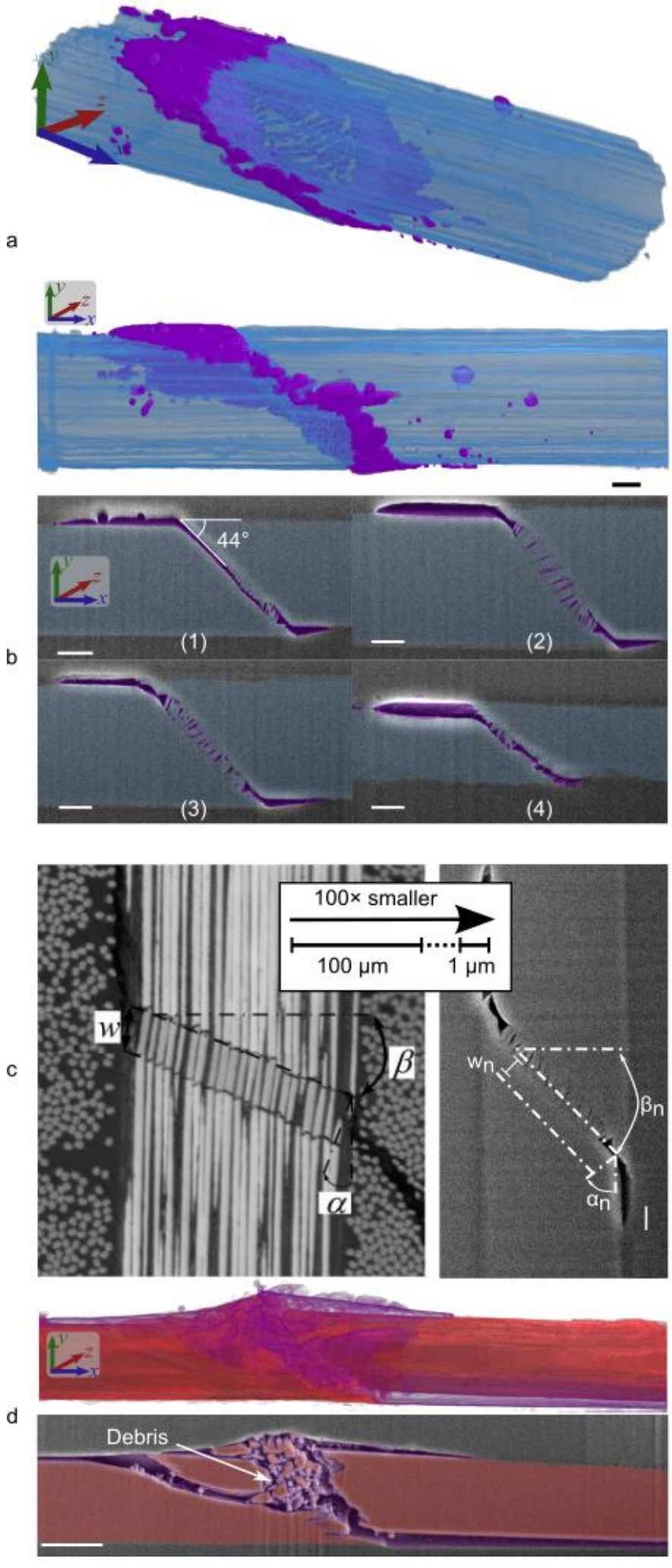

a
b
44°
(1)
(2)
(3)
(4)
c
100× smaller
100 µm
1 µm
w
β
α
wn
βn
αn
d
Debris

Fig. 4 | High modulus internal fibre kink band within a simple break. a. Reconstructed 3D model displaying fibre and void phases from orthographic, side on (xy) view. Fibre displays an average break angle of 44°. b. Regions of interest (ROI)-painted SBF SEM images of sequential slices through sample shown in a. All scale bars in a and b represent 1 μm. Initiation occurred at 0.4% (~2.25 GPa fibre stress), and the sample was deformed to a fibre strain of 0.6 % (~2.46 GPa [6]). As this sample was only deformed to a strain of 0.2% above the initiation point, the debonded lengths and volume are smaller than for previous samples, which were subjected to larger deformations. Debonded lengths are in agreement with the expectation that the failure will progress through the growth of a debond[6]. The void ROI volume was 9.7 μm³, with a maximum debond length of 3.7 μm. The imaged M55J fibre has an asymmetrical "kidney bean" cross-section, commonly observed for M55J fibres[32]. c. Composite fibre kink bands across length scales, where α, β and w are fibre rotation angle, kink band angle and kink band width respectively, with n indicating the same parameters, at the nano scale. SEM image of a composite scale kink band from imaged by Gutkin *et al.,* 2010 [33] with permission from Elsevier. d. High strength (AS4) fibre break morphology, with 3D reconstruction and SEM image with ROI phases overlayed in false colour, scale bar is 5 μm.

Given the self-similarity of the kink band structures formed at different length scales, the parameters used to describe composite-scale kink bands can be applied here to characterise the nano-kink bands, including the fibre rotation angle, α, kink band angle, β, and kink band width, w. For the imaged nano-kink band (where n indicates the internal nano-kink band-scale), $\alpha_n \approx 36 \pm 3°$, $\beta_n \approx 45 \pm 1°$, and $w_n \approx 430 \pm 90$ nm, each measured across 40 randomly selected locations taken from different slices within the same sample set. The angles are comparable to composite values (typically ranging $\alpha \approx$ 20-60° and $\beta \approx$ 20-35°), though β_n is larger.

The absolute kink band width is, necessarily, several orders of magnitude shorter than a typical notched unidirectional (UD) composite sample (15-400 μm)[35,36]. The length of the nanokink band fibre ligaments, which correspond to the kink band width, w_n, together with the transverse ligament width, is highly regular. Kink band splitting is observed within composites; the composite kink band ligament size is not necessarily at the individual fibre scale[37], but often across groups of fibres. Given that the crystallite thickness, L_c, for M55J fibres[20] is approximately 5.6 nm, the kink band ligament width (190 nm) is orders of magnitude larger than individual crystallites. The size and regularity of the nano-kink band ligaments therefore arise from higher-order microstructural or geometric constraints rather than crystallite dimensions alone. Longitudinal kink band splitting in multi-fibre composites occurs in regions of maximum bending, balancing the release of stored elastic energy with the creation of new surfaces[29], leading to interfacial separation of the microstructure. At composite scale, kink band splitting is favoured by a low fibre–matrix interfacial mode II

toughness[1,34]; in nano-kink bands, the fracture is likely associated with the low basal-plane cleavage energy of aligned graphitic planes (~0.37–0.39 J m^{-2})[38]. Since the crystallites are much smaller than the ligaments, and randomly oriented about the fibre axis, the inter-ligament internal fracture can likely find low energy paths between suitable crystallites.

Composite-scale kink bands initiate through matrix yielding at localised axial misalignments, enabling fibre rotation under shear loading[5]. Prior to nano-kink band formation, the graphitic crystallites may already undergo stable elastic rotation, particularly in the more disordered/misaligned core region[20], corresponding to the strain softening observed in compression above ~0.3% strain for M55J fibres[19]. The subsequent nano-kink band forms at an angle, $\beta_n \approx 45°$, close to the plane of maximum resolved shear, and is larger than kink-band angles typically observed in composites ($\beta \approx 20–35°$). At the composite scale, the kink band angle is governed by matrix constraint[4]; the relevant properties for the fibre core are not well determined, but nanoscale splitting indicates relatively little constraint, due to the low strength and toughness of the aligned graphitic planes. β_n then approaches 45° as expected for a shear kink band. The preserved rotation of ordered microstructural segments across the band demonstrates that the failure mode is a shear-kink instability rather than a simple shear fracture. In contrast to composite-scale kink bands, where fibre rotation is constrained by the surrounding polymer matrix, the nano-kink band develops within the carbon-fibre microstructure itself. Shear localisation is therefore controlled by the anisotropic graphitic architecture and its relatively weak shear response. The specific shear properties of the fibre core are not known. However, modelling estimates[39] for the shear strength of the amorphous-carbon/turbostratic-domain regions (~1.86 GPa) are substantially higher than reported[40,41] graphitic interlayer shear strengths (previously reported as low as 1-2.5 MPa, with updated values in the range of 62-140 MPa), suggesting that shear localisation and kink-band formation are more likely to occur within, or along interfaces associated with, the graphitic domains rather than within the disordered carbon phase.

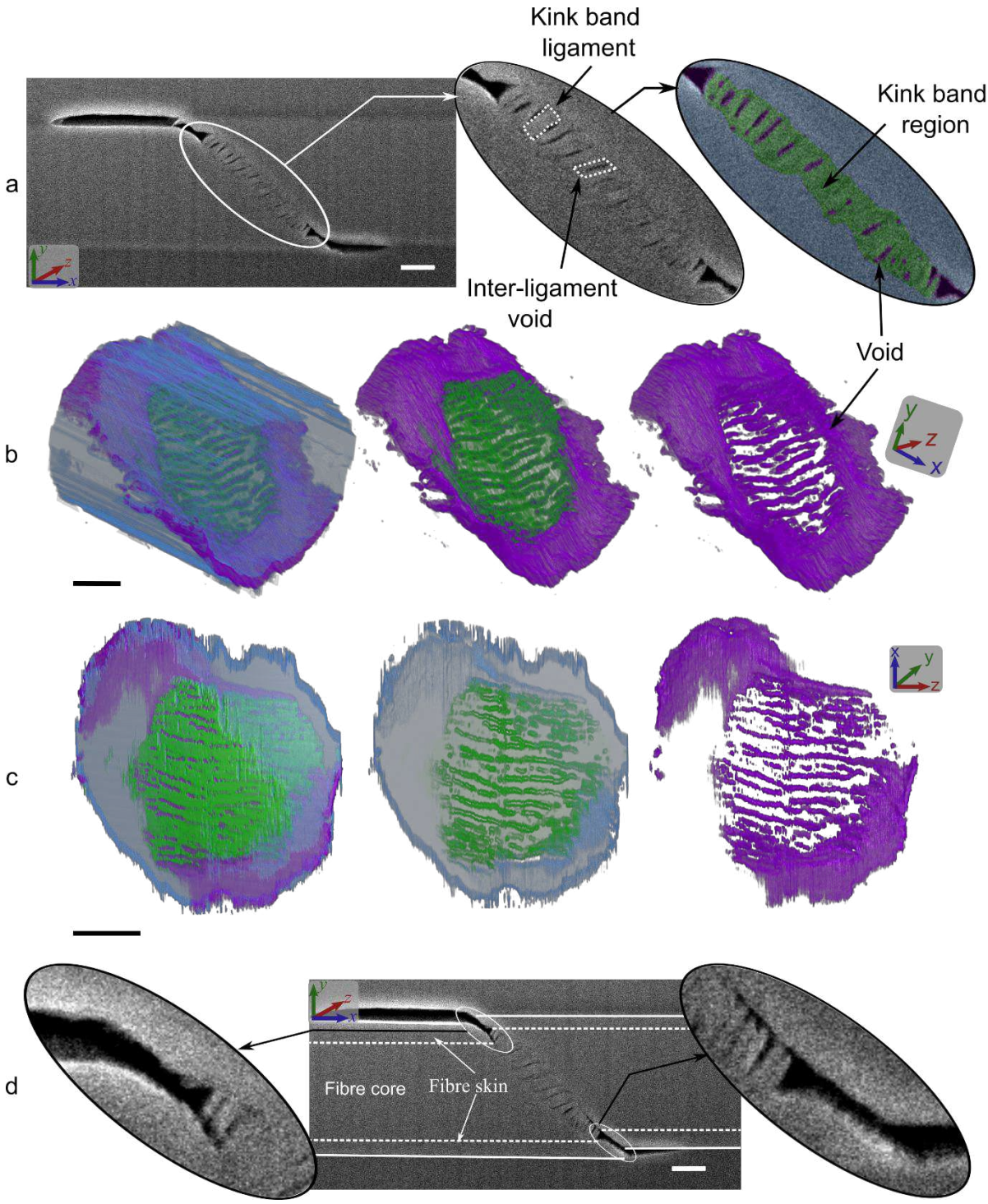


Fig. 5 | Imaging and reconstruction of internal kink band in the M55J fibre. a. SEM images of the kink band at two positions with magnified and region of interest-painted views and measured thicknesses. b. Reconstructed 3D geometry highlighting locally rotated, kink band region, where green is the locally rotated kink band region purple refers to generated void regions about the observed features. c. Orthogonal view of a 0.3 μm thick section reconstructed view of the kink band plane. d. SEM imaging of a kink band cross-section with the indicative location of the skin shown with solid and dotted lines. All scale bars are 1 μm.

The observation of a fracture oriented at approximately 45° to the fibre axis could be misinterpreted as a simple shear-driven failure mode of the fibre. However, the detailed microstructure, resolved

under the strain control of the experiment, highlights the importance of shear instability. Previous studies have proposed that compressive strength is governed by the critical stress required for crystallite kinking within the fibre microstructure[20]. In contrast, the present results indicate that failure is more complex, associated with heterogeneous microstructural features across the fibre diameter. The first indication of failure observed in *is*RSM is a crack in the thin, highly graphitic outer "skin" layer. Although the outer layer is more highly aligned, its shear modulus is likely lower than the core because larger graphitic crystallites increase elastic anisotropy and reduce resistance to interlayer shear[42]. Further, previous studies have suggested that high-modulus PAN-based fibres contain larger longitudinal pores within the skin region[15]. These pores are thought to reduce lateral support for highly aligned crystallites in the skin, promoting failure initiation through shear stresses concentrated near such defects[16]; surface defects or interfacial imperfections may similarly play a role. Although crystallite alignment is higher in the skin than in the core, which would imply higher intrinsic compressive strength based on classical misalignment knockdown arguments[43], the presence and distribution of defects in the skin and lower intrinsic shear modulus favour failure initiation. The absence of any visible kink band formation within the skin further indicates a distinct failure mechanism relative to the core. In the FIB-SEM reconstruction, the fracture surfaces appear to initiate as a microcrack on the fibre surface, highlighted in **Fig. 5**d, reinforcing this interpretation.

The compressive failure initiation process is therefore proposed to proceed through the following sequence. Under increasing compressive deformation, the stress–strain response becomes non-linear as graphitic crystallites undergo elastic rotation, supported by the surrounding disordered carbon phase[20]. Rotation is expected to be more pronounced in the fibre core, where smaller crystallite size, lower crystallite alignment and a higher fraction of disordered carbon allow greater local rotation. This softening redistributes load towards the more highly aligned skin, increasing the local stress carried by this region. Failure then initiates locally within the skin once a critical stress is reached. The axial location of these initial failures is governed by the stochastic distribution of defects, as the first fibre breaks occur only at discrete positions along the fibre length, with later breaks forming progressively under continued loading until fragment saturation is approached. Local defects, such as longitudinal pores, surface defect, regions of reduced lateral support, or areas where highly aligned graphitic crystallites are favourably oriented for basal-plane shear, may act as preferential sites for skin crack initiation.

Once the skin cracks locally, the loss of lateral constraint increases the stress transferred into the more disordered core. The core can then undergo unstable crystallite rotation, *i.e.* nanoscale kinking, which further loads the remaining locally intact surrounding skin and promotes circumferential propagation of the fracture. As the crack develops, the fracture path may inherit the orientation of the internally rotating core due to local stress concentrations. The damaged skin is no longer able

to suppress further local crystallite rotation, allowing an internal nanoscale kink band to form fully. If there is sufficient strain energy, the wedge feature may form through the bifurcation of the circumferentially propagating skin crack. With further deformation, the kink band undergoes additional rotation, fibre fragments begin to slide relative to one another, and kink band ligaments detach from the fibre, as observed in **Fig. 3**. At this stage, inter-fragment contact becomes predominantly frictional, and damage propagation proceeds in accordance with previously reported models[6], with proceeding fragment slip and Mode I debonding. The proposed mechanisms underlying kink band formation are illustrated schematically in Figure S5 (Supplementary Information).

The work here provides the first direct, three-dimensional observation and quantitative description of internal kink-band formation within individual PAN-based carbon fibres under compression. By interrupting failure mid-propagation, we reveal that compressive fracture is governed not by uniform fibre shear or surface damage alone, but by a coordinated hierarchical instability rooted in skin-core microstructural heterogeneity. The identification of failure initiation in the skin coupled with a confined, regularly structured nano-scale kink band within the fibre core, establishes a direct mechanistic link between crystallite-scale rotation, micron-scale fragmentation, and composite-level compressive failure for high modulus fibre composites. These findings challenge prevailing interpretations that attribute fibre compressive strength solely to bulk fibre shear failure or matrix-dominated mechanisms and instead argue that a shear instability arising within fibre skin structures, as well as skin–core microstructural contrast dictates failure initiation and propagation. Rotational compliance[44] of the core leads to sufficient stress and strain in the skin to initiate failure where the structure is weakest in shear, which then drives further rotation within the core crystallites. By bridging length scales and directly visualising internal failure modes, this study provides a new route to understanding and improving compressive performance in carbon fibres and their composites.

Failure observed in high strength fibres

The failure morphology of HS fibres is markedly different to HM fibres (see **Fig. 4** d and Fig. S4, Supplementary information). HM fibres fail at low strains with limited stored elastic energy, allowing more progressive fracture events, shorter interfacial debonded lengths, and reduced damage to the surrounding matrix. Fibre driven failure is also manifested in high modulus fibre bulk composites[23]. In contrast, HS fibres accumulate an order of magnitude greater elastic energy before failure, failing at much higher compressive strains (2.2 % for AS4 vs 0.5 % for M55J[19]). Rapid energy release then drives extensive post-failure deformation, including wider fracture zones, multiple fragmentation planes, and the formation of debris and interfacial damage, resembling classic brittle failure. The initiation likely still involves nanoscale shear instability, due to the high anisotropy with the fibres, but cannot be followed progressively. In bulk composites, HS fibres do not usually reach this failure

strain, as micro-scale matrix shear instability occurs first, leading to conventional composite kink-band formation. The origin of the higher compression strength for HS fibres must lie in their microstructure. Although the graphitic crystallites in HS fibres are less well aligned, which is conventionally associated with reduced resistance to shear instability, they are also less graphitised, implying greater shear strength. The implication is that fibre compression strength is driven by shear strength and modulus, analogously to the matrix dependence of composites in compression. Measurements of fibre shear strength, especially resolved spatially across the fibre diameter (skin/core), are rare and hard to interpret, due to the complex nature of the experiment[45]. Methods to improve shear strength in highly aligned (HM) fibres would be expected to increase the compression strength of both fibres and their composites.

Discussion and outlook

Compressive failure in carbon-fibre-reinforced composites is commonly described in terms of matrix shear instability and fibre microbuckling at the composite scale. For high-modulus PAN-based fibre composites, failure is instead governed by intrinsic fibre failure; however, the results here demonstrate that similar microstructural instability mechanisms are responsible, but operating at characteristic length scales that are two orders of magnitude smaller. The interaction between regions with varying microstructures within the fibre cross-section is also reminiscent of longer length-scale interactions in composite structures, where kink-band initiation is often associated with correlated variations in fibre orientation[46], ply lay-up, ply drops, voids, or notches[29]. At the micron scale, compressive failure is characterised by fibre fragmentation, wedge formation, interfacial debonding, and void generation.

The presence of mode I debonding introduces an additional toughening mechanism in compression that has not been previously reported. Since interfacial failures are usually associated with mode II shear yielding, this alternative mechanism may have significant implications for designing interfaces tailored for compressive applications[19]. Conventional fibre-matrix interface engineering in composites uses surface chemistry to improve adhesion and hence shear strength. Whilst increasing adhesion will also limit mode I failure, additional features could provide targeted benefits. Specifically, for example, the use of ‘fuzzy fibres’, grafted with carbon nanotubes (CNTs)[47], could provide an additional bridging mechanism to limit interfacial crack opening. CNT-modified carbon fibre composites have been reported to deliver substantial improvements in compression-related performance, with fibre-direction compressive strength increases of ~20% and modelled interphase shear modulus increases approaching ~30%[48]. In HS CF composites the effect is usually attributed to increased matrix shear strength, helping to resist kink band initiation. Here, an additional mechanism is identified in HM composites in compression[19], which may improve post-fragmentation toughness, delaying fragment evolution.

Combining observations made using *is*RSM, optical microscopy and FIB-SEM SBF imaging suggest a failure sequence in which elastic rotation of graphitic crystallites produces the non-linear compressive stress–strain response observed prior to failure. Failure first initiates in the fibre skin, where higher graphitic crystallite alignment has inherently lower shear strength, leading to basal-plane shear and surface microcracking. The resulting loss of lateral constraint enables shear-driven buckling of the more compliant, disordered core microstructure, giving rise to internal kink-band formation. Nanoscale kink bands exhibit well-defined rotation angles, widths, and orientations that closely mirror those observed in composite-scale kink bands, despite occurring entirely within a single fibre. The confinement of kink bands to the fibre core, alongside the absence of such features in the skin, provides significant evidence that radial microstructural heterogeneity plays a decisive role in compressive failure. With continued deformation, these kink bands undergo further rotation, fragment interaction becomes frictional, and macroscopic fibre fragmentation ensues.

This work shows that shear instability is as relevant to compressive failure at the nanoscale as it is at the microscale. In composites that fail by intrinsic fibre failure, particularly high-modulus systems, improvements in compressive performance may therefore be gained by addressing fibre-scale instabilities that lead to nano-kink-band formation. In high-strength composites, where compressive failure is more commonly dominated by composite-scale micro-kink bands, matrix and interface optimisation remain essential. However, once composite-scale microbuckling is suppressed, similar fibre-scale instability mechanisms may become increasingly important. This argument indicates that compression performance should not be considered solely as a laminate, matrix, or interface design problem, but also as a fibre-microstructure and fibre-manufacturing problem, across a large range of lengthscales.

The observation of intrinsic nanoscale kink-band formation suggests that carbon fibres contain internal structural features capable of localising shear instability. Boll *et al.* previously suggested that crystallite dimensions should be limited to below 5 nm whilst maintaining good orientation to strengthen fibres in compression[49], but in addition, we suggest that additional future gains in compressive strength may also require deliberate control of radial microstructural heterogeneity, crystallite alignment, skin–core contrast, and local shear resistance within the fibre. Processing routes that modify precursor alignment, stabilisation, carbonisation, graphitisation, or surface treatment may influence not only tensile modulus and strength, but also the fibre's resistance to internal compressive instability. In this sense, the fibre should be treated not simply as a homogeneous reinforcement, but as a hierarchical material whose internal architecture controls its failure response. From an applications perspective, these findings are important because compression remains one of the limiting design cases for high-performance composite structures.

A better understanding of intrinsic fibre compression failure could therefore contribute to lighter, more reliable, and more resource-efficient composite structures.

The balancing of similar deformation and failure mechanisms across different structural length scales is a familiar feature of natural hierarchical materials, including bone and wood[50]. In these systems, properties emerge from interactions between architecture, interfaces, anisotropy, and local failure mechanisms across multiple scales. The present results suggest that carbon-fibre composites should be considered in a similar hierarchical framework: not only as assemblies of fibres, plies, laminates, and components, but as systems in which the reinforcing fibres themselves contain critical internal structural hierarchy. Recognising this hidden hierarchy changes the length scale at which compressive failure must be understood and offers new opportunities for material design.

Future work should extend this approach across a wider range of fibre chemistries, moduli, precursor routes, graphitisation conditions, surface treatments, and matrix systems. Larger statistical datasets would allow the relative roles of fibre modulus, crystallite alignment, radial heterogeneity, interface strength, and matrix constraint to be separated more clearly. *In situ* or interrupted-loading studies would also be valuable for directly capturing the transition from reversible crystallite rotation, to skin cracking, to internal kink-band formation, and finally to fragmentation. Such studies could establish whether nanoscale kink-band formation is a general feature of high-modulus carbon-fibre compression, or whether it can be suppressed through targeted fibre or interface design.

This work moves the understanding of carbon-fibre compressive failure from indirect inference towards direct three-dimensional observation. Rather than viewing fibre failure as the final outcome of composite compression, the fibre can now be understood as an active hierarchical material that undergoes its own internal instability sequence. Controlling this sequence offers a route towards carbon fibres and composite architectures optimised not only for tensile stiffness and strength, but also for resistance to compression-driven instability.

Methods

Specimen preparation

The epoxy resin formulation used was a two-part resin system, consisting of Araldite® LY5052 containing 50-70 % phenol polymer with formaldehyde, glycidyl ether and 30-50% 1,4-bis(2,3-epoxypropoxy)butane, and a hardener, Aradur® 5052CH, containing 50-70% 2,2’dimethyl-4,4’-methylenebis(cyclohexylamine), 30-50% 3-aminomethyl-3,5,5-trimethylcyclohexylamine, 3-5%, 2,4,6-tris(dimethylaminomethyl)phenol and 1-3% salicylic acid. Both the resin and the hardener were purchased from Silmid (Birmingham, UK). This resin system had a low viscosity which allowed mixing and manipulation at room temperature. Epoxy prisms were cast in silicone moulds, producing

12 × 6 × 6 mm^3 specimens, by thoroughly mixing the resin components, LY5052 and 5052CH, in a ratio of 100:38 parts by weight, following the manufacturer's guidelines. The resin mixture was degassed at 700 mm.Hg. for 30 minutes. The silicone mould was coated with Ambersil Formula 10 release agent (RS Components Ltd, Bristol, GB) to aid the removal of epoxy once cured, applied via aerosol spray. The degassed epoxy solution was poured into the mould and left at room temperature and ambient conditions for 7 days to allow the prisms to cold cure. Once cured, the prisms were removed from the silicone mould, and excess cured epoxy was removed using abrasive sandpaper.

A secondary epoxy layer was used to embed single fibres into the surface of the prisms. The two epoxy resin components were mixed in the same ratio and degassed under the same conditions. Once the mixture was degassed, the solution was thinned by adding acetone to the epoxy, in a ratio of 25:75 parts by weight epoxy to acetone.

The carbon fibres used in this study were PAN based carbon fibre. High modulus fibres used were M55J (M55JB-6000-50B, Lot No: F212OH2) fibres were purchased from Toray (Nijverdal, NL). Intermediate modulus fibres used were unsized AS4 HS-CP-5000 carbon fibres used as received, supplied by Hexcel Composites (Hexcel GB).

Small bundles of carbon fibres were removed from fibre tows and cut into short (3-5 mm) lengths with a scalpel. Short fibres were manipulated onto the surface of the previously cured prisms, aligned parallel and centrally with its long edge, and secured in place with adhesive tape. Acetone thinned epoxy was then drop casted over the fibre using an adjustable air-displacement pipette in a volume of 30 µL, having removed the adhesive tape prior to this step. For the unsized AS4 fibre samples, 15 µL was used to further reduce the epoxy thickness for increased sensitivity for Raman analysis due to reduced mode intensity due to lower overall graphitic nature.

The drop-cast solution was spread out evenly over the prism's surface to ensure uniform film thickness over the surface of the fibre. The fibre was also gently manipulated with tweezers to ensure alignment with the prism's long edge if any drift occurred during the drop casting step. Acetone in the epoxy evaporated rapidly, leaving a resin layer over the fibres. Embedded fibre samples were kept at room temperature and pressure for 7 days to allow cold curing to occur to minimise residual stresses acting on the fibre. The samples were subjected to a post-cure step of 60 °C for 6 h at ambient pressure to ensure consistent curing across sample batches. C4A Series linear strain gauges (C4A-06-015SLA-120-39P) with gage factors of 1.88 were purchased from Micro-Measurements group (Basingstoke, GB) and adhered to epoxy prisms utilising cyanoacrylate adhesive (Technimeasure Doncaster, GB), used to monitor deformation.

Resulting prisms had a single embedded fibre within 50 µm of the epoxy's surface, aligned with the long edge of the prism, in the centre of the face.

Sample deformations

Single fibre model composites were subjected to uniaxial compression utilising a Deben MICROTEST tensile compression stage, fitted with a 5 kN loadcell. The epoxy prisms are placed between the grips and compression is applied incrementally at a crosshead displacement rate of 0.1 mm/min, in matrix compressive strain steps of 0.034%. Strain gauges were monitored using a Micro-measurements D4 Data Acquisition Conditioner, giving matrix strain values. Samples were monitored during loading with optical microscopy and Raman spectroscopy, as detailed elsewhere[6].

Optical microscopy

Optical microscopy images were taken using a Euromex bScope® metallurgical microscope coupled with a VC.3040 UHD-4K camera and processed in ImageJ (Fiji, ver. 2.16.0).

SEM sample preparation

Once samples have been subjected to compressive deformation to the required state, the samples were unloaded. Fibre break features ROIs were imaged with optical microscopy. The positions of the ROIs were measured relative to the fibre's length and local surface features, to aid with finding the features in the SEM.

Samples were then mounted on SEM stubs via an adhesive carbon pad (purchased from Agar Scientific Ltd, GB). A transmission electron microscopy (TEM) copper sample grid was adhered over the fibre's position on the surface of the epoxy and imaged with optical microscopy to ensure the position of the fibre relative to the grid was known. A gold layer was then sputtered over the surface of the prism, with the TEM grid adhered using adhesive tape to the surface. Gold was deposited to aid sample conductivity for layer SEM imaging. Silver DAG was used to bridge the surface gold layer to the carbon adhesive pad. The TEM grid was then removed from the surface of the prism, leaving a negative pattern of the grid on the surface from the gold sputtering. An additional, thin layer of gold was sputtered over the prisms' surface to ensure that the region pattern location was also conductive, whilst maintaining the TEM grid pattern.

These steps were taken to aid sample conductivity for imaging in SEM and to aid with finding the carbon fibre under the surface of the epoxy. The resulting sample, ready for FIB-SEM analysis was a single mounted prism with a gold sputtered layer, marked with a TEM grid, which the fibre's location was noted and ROIs were measured with reference to the grid and local surface features with optical microscopy.

FIB-SEM region of interest preparation

A Thermo Fisher Scientific Helios 5 Hydra Plasma FIB (PFIB) operating with O_2 gas at 30 kV was used for serial sectioning. The PFIB column had an ion beam current range of 1.5 pA to 2.5 µA with an acceleration voltage range of 500 V – 30 kV. SEM components included a FEG electron source

with 350 V – 30 kV acceleration voltage, with an in-lens SE/BSE detector and Everhart-Thornley SE detectors.

The first stage of imaging involved determining the fibre's position, and alignment. During milling, the stage was tilted so the ion beam was perpendicular to the surface, while the electron beam was angled at 52° to the surface. Ion beam conditions of 45 nA and 1.9 µA at 30 kV were employed to mill the epoxy gradually. Using the ion beam column's reduced-area imaging mode under these conditions, trenches were selectively etched into the epoxy approximately 50 µm away from a known ROI to avoid disturbing the feature of interest. Careful monitoring with both the electron and ion imaging beams imaging ensured the trenches were milled until the fibre was exposed. This process was repeated on the opposite side of the position of interest (POI), exposing the fibre on both sides. The stage was then aligned relative to the beam using the two exposed sections. A fibre end was typically located initially, using the reduced area imaging method, providing a positional reference for identifying the position of the ROI. Once the fibre was located and the ROI position identified estimated from prior measurements, a thin (<1 µm) tungsten (W) protective layer was selectively deposited over the epoxy surface at the POI location. This marked the ROI, protected the region from accidental damage and for improved imaging quality during FIB milling.

Imaging and side trenches were then milled surrounding the ROI to a depth well below the fibre's depth. Optimal fibre depths for high-quality, well resolved sectioning images ranged from 10–30 µm. Beyond 30 µm, the sectioning time exceeded 12 h with a lower imaging resolution. The purpose of these trenches was to expose the imaging face to the SEM detector view and for milled material to re-deposit away from the ROI. Imaging and milling fiducials were milled into the epoxy, preferably on W-coated sections to maximise imaging contrast. These fiducials were essential for the Thermo Fisher Auto Slice-and-View sectioning, allowing automatic positional adjustments during the slice-and-view process.

Slice-and-view milling

To section the prepared ROI, Thermo Fisher Scientific's Auto Slice & View 5 software was used. The programme sets milling and imaging parameters and automatically adjusts the stage position using fiducial markers to account for the focal plane movement as material was removed. By adjusting the milling depth, slice thickness, and imaging parameters, the voxel size and processing time was controlled. Generally, a minimum voxel size is typically desired whilst maintaining a reasonable total milling and imaging time of under 15 hours. Voxel sizes ranged from 10 × 12.7 × 10 nm^3 to 40 × 50.76 × 50 nm^3 (x × y × z).

The slice-and-view process removed a layer of the ROI with a polishing mill pass, followed by SEM imaging, and was repeated for the set milling thickness. Autofocus was applied with each frame for

optimal image quality. The output was a stack of SEM images collected imaged with an Everhart-Thornley detector (ETD).

Image stack treatment and segmentation

To analyse and process SEM image stacks obtained from FIB-SEM milling, ImageJ (Fiji, ver. 2.16.0) and Dragonfly 3D World (Comet Technologies Canada Inc. Dragonfly 3D World. version 2024.1, Comet Technologies Canada Inc., 2024, https://dragonfly.comet.tech/., build 1601) were used for image segmentation.

The image stack was first trimmed to only include the images with the ROI in frame, reducing the number of images in the stack. The trimmed stack was imported into ImageJ and the images in the stack are cropped to a minimum, still with the features of interest in frame. ImageJ pre-treatment then focused on maximizing the contrast between the fibre, voids, and the matrix. The brightness-contrast ratio was tuned to improve contrast in the images. A Gaussian blur filter with a standard deviation value (sigma value) of 2-3 was applied to reduce noise and improve contrast without sacrificing fine details, aiding effective segmentation.

The cropped and ImageJ-treated stack was imported into Dragonfly, where inbuilt AI-assisted automatic segmentation models were used to process stacks of images (typically 400-700 images). A U-Net-based deep learning architecture, designed to analyse visual imagery, was trained to segment the stack. U-Net is particularly effective at handling noisy images and artifacts. The model was trained by annotating 5-10 example images, defining the ROIs as the fibre, void, and matrix (background). Once trained, the model was able to segment the entire stack, with manual review and corrections made as necessary. The accuracy of automatic segmentation improves with higher contrast between phases. The fully segmented stack was then visually analysed in 3D, allowing for detailed observations of fibre breaks that may not be visible in the 2D stack.

Data Availability

Supporting data can be requested from the corresponding author but may be subject to confidentiality obligations. For the purpose of open access, the authors have applied a Creative Commons Attribution (CC-BY) license to any author accepted manuscript version arising.

References

1. Fleck, N. A. Compressive Failure of Fiber Composites. in *Advances in Applied Mechanics* vol. 33 43–117 (1997).
2. Ennis, B. L. *et al.* Optimized Carbon Fiber Composites in Wind Turbine Blade Design. *Sandia Rep.* 1–69 (2019).
3. Nunna, S., Ravindran, A. R., Mroszczok, J., Creighton, C. & Varley, R. J. A review of the

structural factors which control compression in carbon fibres and their composites. *Compos. Struct.* **303**, 116293 (2023).

4. Budiansky, B. & Fleck, N. A. Compressive failure of fibre composites. *J. Mech. Phys. Solids* **41**, 183–211 (1993).
5. Pimenta, S., Gutkin, R., Pinho, S. T. & Robinson, P. A micromechanical model for kink-band formation: Part I - Experimental study and numerical modelling. *Compos. Sci. Technol.* **69**, 948–955 (2009).
6. Woodgate, C. G., Trask, R. S., Shaffer, M. S. P. & Eichhorn, S. J. Raman spectroscopic stress mapping of single high modulus carbon fibre composite fragmentation in compression. *Compos. Sci. Technol.* **255**, 110721 (2024).
7. Ghaffari, S., Seon, G. & Makeev, A. Effect of Fiber–Matrix Interface Friction on Compressive Strength of High-Modulus Carbon Composites. *Molecules* **28**, (2023).
8. Pohlkemper, F., Rolfes, S., Bouhrara, M., Röding, T. & Gries, T. Market analysis of carbon fiber production with reference to the oxidation ovens used. *Appl. Res.* **3**, (2024).
9. Paris, O. & Peterlik, H. *The Structure of Carbon Fibres*. *Handbook of Textile Fibre Structure* vol. 2 (Woodhead Publishing Limited, 2009).
10. Wang, J., Salim, N., Fox, B. & Stanford, N. Anisotropic compressive behaviour of turbostratic graphite in carbon fibre. *Appl. Mater. Today* **9**, 196–203 (2017).
11. Huang, Y. & Young, R. J. Effect of fibre microstructure upon the modulus of PAN- and pitch-based carbon fibres. *Carbon N. Y.* **33**, 97–107 (1995).
12. Bennett, S. C., Johnson, D. J. & Johnson, W. Strength-structure relationships in PAN-based carbon fibres. *J. Mater. Sci.* **18**, 3337–3347 (1983).
13. Nunna, S. *et al.* The effect of thermally induced chemical transformations on the structure and properties of carbon fibre precursors. *J. Mater. Chem. A* **5**, 7372–7382 (2017).
14. Johnson, D. J. Structure-property relationships in carbon fibres. *J. Phys. D. Appl. Phys.* **20**, 286–291 (1987).
15. Bennett, S. C. & Johnson, D. J. Electron-microscope studies of structural heterogeneity in pan — based carbon fibres. *Composites* **10**, 240 (1979).
16. Oya, N. & Johnson, D. J. Longitudinal compressive behaviour and microstructure of PAN-based carbon fibres. *Carbon N. Y.* **39**, 635–645 (2001).
17. Tanaka, F., Okabe, T., Okuda, H., Kinloch, I. A. & Young, R. J. Factors controlling the strength of carbon fibres in tension. *Compos. Part A Appl. Sci. Manuf.* **57**, 88–94 (2014).
18. Bennett, S. C. & Johnson, D. J. Fifth London International Carbon and Graphite Conference. *Soc. Chem. Ind. London* **377**, (1978).

19. Woodgate, C. G., Anthony, D. B., Trask, R. S., Shaffer, M. S. P. & Eichhorn, S. J. Raman spectroscopic stress mapping of carbon nanotube coated single high modulus carbon fibres in compression. *Compos. Sci. Technol.* **270**, 111283 (2025).

20. Tanaka, F., Okabe, T., Okuda, H., Kinloch, I. A. & Young, R. J. The effect of nanostructure upon the compressive strength of carbon fibres. *J. Mater. Sci.* **48**, 2104–2110 (2013).

21. Nakatani, M., Shioya, M. & Yamashita, J. Axial compressive fracture of carbon fibers. *Carbon N. Y.* **37**, 601–608 (1999).

22. Sugimoto, Y., Shioya, M., Yamamoto, K. & Sakurai, S. Relationship between axial compression strength and longitudinal microvoid size for PAN-based carbon fibers. *Carbon N. Y.* **50**, 2860–2869 (2012).

23. Suwarta, P., Czél, G., Fotouhi, M., Rycerz, J. & Wisnom, M. R. Pseudo-ductility of unidirectional thin ply hybrid composites in longitudinal compression. *33rd Tech. Conf. Am. Soc. Compos. 2018* **2**, 1032–1041 (2018).

24. Ghaffari, S. *et al.* Understanding compressive strength improvement of high modulus carbon-fiber reinforced polymeric composites through fiber-matrix interface characterization. *Mater. Des.* **193**, 108798 (2020).

25. Boll, D. J., Jensen, R. M., Cordner, L. & Bascom, W. D. Compression Behavior of Single Carbon Filaments Embedded in an Epoxy Polymer. *J. Compos. Mater.* **24**, 208–219 (1990).

26. Cheng, H. & Zhou, X. An energy-based criterion of crack branching and its application on the multidimensional space method. *Int. J. Solids Struct.* **182**–**183**, 179–192 (2020).

27. Pickering, K. L. & Murray, T. L. Weak link scaling analysis of high-strength carbon fibre. *Compos. Part A Appl. Sci. Manuf.* **30**, 1017–1021 (1999).

28. Guo, X. *et al.* New insights into orientation distribution of high strength polyacrylonitrile-based carbon fibers with skin-core structure. *Carbon N. Y.* **109**, 444–452 (2016).

29. Wang, Y. *et al.* X-ray computed tomography study of kink bands in unidirectional composites. *Compos. Struct.* **160**, 917–924 (2017).

30. Dobb, M. G., Johnson, D. J. & Park, C. R. Compressional behaviour of carbon fibres. *J. Mater. Sci.* **25**, 829–834 (1990).

31. Dobb, M. G., Johnson, D. J. & Saville, B. P. Compressional behaviour of Kevlar fibres. *Polymer (Guildf).* **22**, 960–965 (1981).

32. Khayyam, H. *et al.* PAN precursor fabrication, applications and thermal stabilization process in carbon fiber production: Experimental and mathematical modelling. *Prog. Mater. Sci.* **107**, 100575 (2020).

33. Gutkin, R., Pinho, S. T., Robinson, P. & Curtis, P. T. On the transition from shear-driven fibre

compressive failure to fibre kinking in notched CFRP laminates under longitudinal compression. *Compos. Sci. Technol.* **70**, 1223–1231 (2010).

34. Prabhakar, P. & Waas, A. M. Interaction between kinking and splitting in the compressive failure of unidirectional fiber reinforced laminated composites. *Compos. Struct.* **98**, 85–92 (2013).
35. Wang, Y., Chai, Y., Soutis, C. & Withers, P. J. Evolution of kink bands in a notched unidirectional carbon fibre-epoxy composite under four-point bending. *Compos. Sci. Technol.* **172**, 143–152 (2019).
36. Srisuriyachot, J. *et al.* Synchrotron micro-CT in kink-band formation of UD-CFRP laminates with microdefects. *Compos. Part B* **266**, 111038 (2023).
37. de Castro Pimenta, S. A. O. Micromechanics of Kink-Band Formation. (Universidade do Porto (Portugal), 2008).
38. Wang, W. *et al.* Measurement of the cleavage energy of graphite. *Nat. Commun.* **6**, 7853 (2015).
39. Naraghi, M. & Chawla, S. Carbonized Micro- and Nanostructures: Can Downsizing Really Help? *Materials (Basel).* **7**, 3820–3833 (2014).
40. Wang, Y. *et al.* Intrinsic interlayer shear strength of graphite. *J. Mech. Phys. Solids* **193**, 105853 (2024).
41. Liu, Z. *et al.* Interlayer shear strength of single crystalline graphite. *Acta Mech. Sin.* **28**, 978–982 (2012).
42. Shirasu, K., Goto, K. & Naito, K. Microstructure-elastic property relationships in carbon fibers: A nanoindentation study. *Compos. Part B Eng.* **200**, 108342 (2020).
43. Wisnom, M. R. The effect of fibre misalignment on the compressive strength of unidirectional carbon fibre/epoxy. *Composites* **21**, 403–407 (1990).
44. Shioya, M. & Takaku, A. Rotation and extension of crystallites in carbon fibers by tensile stress. *Carbon N. Y.* **32**, 615–619 (1994).
45. Liu, D., Peng, K. & He, Y. Direct measurement of torsional properties of single fibers. (2016) doi:10.1088/0957-0233/27/11/115017.
46. Wilhelmsson, D., Mikkelsen, L. P., Fæster, S. & Asp, L. E. Influence of in-plane shear on kink-plane orientation in a unidirectional fibre composite. *Compos. Part A* **119**, 283–290 (2019).
47. Sahu, R., Ponnusami, S. A., Weimer, C. & Harursampath, D. Interface engineering of carbon fiber composites using CNT: A review. *Polym. Compos.* **45**, 9–42 (2024).
48. Almousa, H., De Luca, H., Anthony, D., Greenhalgh, E. & Bismarck, A. How can hierarchical composites with carbon nanotube-grafted carbon fibres enhance compression performance?

in *Proceedings of the 21st European Conference on Composite Materials* 734–740 (2024). doi:https://www.dx.doi.org/10.60691/yj56-np80.

49. Dobb, M. G., Guo, H., Johnson, D. J. & Par, C. R. Structure-compressional property relations in carbon fibres. *Carbon N. Y.* **33**, 1553–1559 (1995).

50. Huang, W. *et al.* Multiscale Toughening Mechanisms in Biological Materials and Bioinspired Designs. *Adv. Mater.* **31**, 1–37 (2019).

Acknowledgements

The authors would also like to acknowledge the use of facilities within the Interface Analysis Centre and for access to the Hydra PFIB, funded by the EPSRC Grant EP/W036576/1.

Author Contribution

C.G.W. contributed to conceptualisation, methodology, formal analysis, validation, investigation, data curation, visualisation, writing the original draft, and reviewing and editing the manuscript. D.B.A. contributed to conceptualisation, methodology, project administration, and reviewing and editing the manuscript. C.P.J. contributed to FIB-SEM methodology and investigation. S.J.E. contributed to conceptualisation, supervision, and funding acquisition. M.S.P.S. contributed to conceptualisation, supervision, and funding acquisition. All authors reviewed and approved the final manuscript.

Funding

The authors kindly acknowledge the funding for this research provided by UK Engineering and Physical Sciences Research Council (EPSRC) programme Grant EP/T011653/1, Next Generation Fibre-Reinforced Composites (NextCOMP): a Full Scale Redesign for Compression a collaboration between Imperial College London and the University of Bristol.

Competing Interest Statement

The authors declare no competing interests.

Supplementary Files

This is a list of supplementary files associated with this preprint. Click to download.

- CWoodgateESICommMaterFINAL.docx